

Mechanical Characterization of Structured Sheet Materials

CHRISTIAN SCHUMACHER, Disney Research and ETH Zurich

STEVE MARSCHNER, Cornell University

MARKUS GROSS, Disney Research and ETH Zurich

BERNHARD THOMASZEWSKI, Université de Montréal

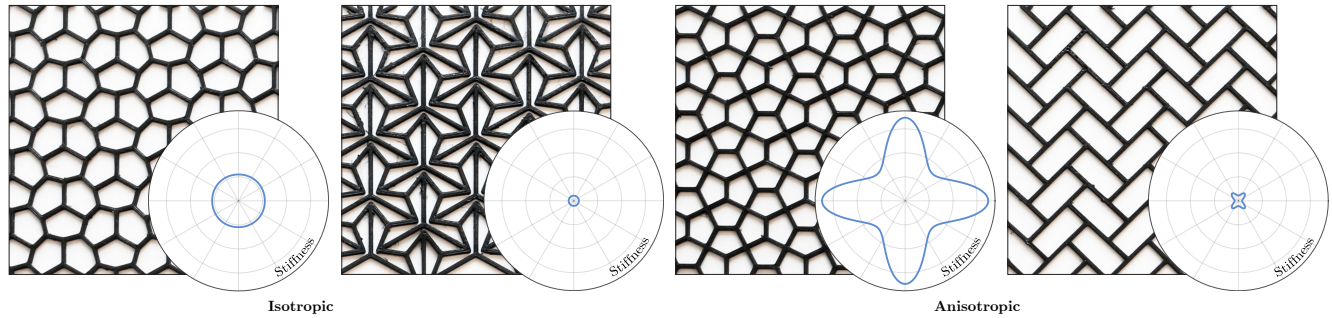


Fig. 1. 3D-printed tilings combine aesthetically-pleasing geometry with complex mechanical behavior characterized by anisotropy, nonlinearity, and large variations in stiffness among different patterns. Using numerical homogenization, our method summarizes the macro-mechanical behavior of these tilings in terms of direction-dependent Young's modulus (shown above), Poisson's ratio, and bending stiffness as well as a simple measure of nonlinearity.

We propose a comprehensive approach to characterizing the mechanical properties of structured sheet materials, i.e., planar rod networks whose mechanics and aesthetics are inextricably linked. We establish a connection between the complex mesoscopic deformation behavior of such structures and their macroscopic elastic properties through numerical homogenization. Our approach leverages 3D Kirchhoff rod simulation in order to capture nonlinear effects for both in-plane and bending deformations. We apply our method to different families of structures based on isohedral tilings—a simple yet extensive and aesthetically interesting group of space-filling patterns. We show that these tilings admit a wide range of material properties, and our homogenization approach allows us to create concise and intuitive descriptions of a material's direction-dependent macromechanical behavior that are easy to communicate even to non-experts. We perform this characterization for an extensive set of structures and organize these data in a material browser to enable efficient forward exploration of the aesthetic-mechanical space of structured sheet materials. We also propose an inverse design method to automatically find structure parameters that best approximate a user-specified target behavior.

CCS Concepts: • **Applied computing** → **Computer-aided design**;

Additional Key Words and Phrases: Mechanical Characterization, Space-Filling Tiling

Permission to make digital or hard copies of all or part of this work for personal or classroom use is granted without fee provided that copies are not made or distributed for profit or commercial advantage and that copies bear this notice and the full citation on the first page. Copyrights for components of this work owned by others than the author(s) must be honored. Abstracting with credit is permitted. To copy otherwise, or republish, to post on servers or to redistribute to lists, requires prior specific permission and/or a fee. Request permissions from permissions@acm.org.

© 2018 Copyright held by the owner/author(s). Publication rights licensed to ACM. 0730-0301/2018/8-ART148 \$15.00

<https://doi.org/10.1145/3197517.3201278>

ACM Reference Format:

Christian Schumacher, Steve Marschner, Markus Gross, and Bernhard Thomaszewski. 2018. Mechanical Characterization of Structured Sheet Materials. *ACM Trans. Graph.* 37, 4, Article 148 (August 2018), 15 pages. <https://doi.org/10.1145/3197517.3201278>

1 INTRODUCTION

Simple shapes can combine into structures of fascinating regularity and complexity. Thanks to their aesthetic appeal and diversity, such *tessellations* are used as a universal way of decorating buildings, garments, and everyday things across many cultures. But the diversity created by these patterns is not limited to appearance. Just as aesthetic complexity can be created from simple shapes, so can mechanical complexity. Indeed, physical representations of these patterns—which we call *structured sheet materials*—exhibit a wide range of macromechanical properties mediated only by geometry and topology. Unlike appearance, however, the mechanical properties of structured sheet materials are often far from obvious. Exploring and understanding the connection between the geometry and mechanics of structured sheet materials is the main objective of this work.

The graphics community has recently started to explore the design of flexible materials whose microstructure can be controlled in order to achieve desired macroscopic deformation behavior [Bickel et al. 2010; Martínez et al. 2016; Panetta et al. 2015; Schumacher et al. 2015]. While previous work has so far focused on volumetric materials, our structured sheets are planar networks of thin elastic rods that can stretch and *bend*. We focus on isohedral polygonal tilings, a particular class of periodic patterns in which all tiles are congruent to a single polygon. Polygonal tilings have been studied intensively in mathematics [Grünbaum and Shephard 1986] and graphics [Kaplan 2009]. We show that this geometrically rich space

of patterns offers an equally varied range of mechanical properties, characterized by strong anisotropy and nonlinearity for both stretching and bending deformations.

The space of isohedral polygonal tilings is partitioned into a set of distinct families, each of which admits certain tileability-preserving transformations on the tile shape. Parameterizing these shapes within a given family yields a continuous sub-space of aesthetically pleasing patterns of the same topology but potentially vastly different mechanical properties. From a user perspective, however, finding a pattern that exhibits desired mechanical properties while satisfying aesthetic criteria is difficult because of the highly unintuitive relation between structure and mechanics. Our goal is to characterize the macromechanical properties of these structures in a concise and intuitive way so as to allow for an informed exploration of the design space.

To this end, we propose a homogenization approach that maps the mechanical behavior of a meso-scale network of elastic rods to a macro-scale thin plate model, making deliberate choices about which properties to capture and communicate. We compute a large set of deformations for each rod network and optimize for the tensors describing the anisotropic stretching and bending behavior of the sheet such that, around a given state of deformation, the thin plate model best approximates the large-scale properties of the rod network. Even though our model is only a partial description and approximation of the true material behavior, a good qualitative agreement between the meso-scale and macro-scale properties is found even for large deformations. The rather extensive material data of the thin plate model is distilled into a compact visual representation in terms of directional Young's moduli, Poisson's ratios, bending stiffnesses, and corresponding measures of nonlinearity. We organize the resulting representations in a dedicated material browser, allowing users to explore the space of polygonal tilings with respect to both aesthetic and mechanical properties.

Apart from the geometry and topology of the patterns, our homogenization method only requires the mechanical properties of the base material as input. For the purpose of experimental validation, we 3D print a set of pattern prototypes and measure stress-strain and moment-curvature profiles. Our results show very good agreement between the physical prototypes and their simulated counterparts, even for large deformations with substantial buckling.

2 RELATED WORK

Designing Structured Materials. With the increased accessibility of additive manufacturing technologies and new possibilities in fabricating complex geometries, the design and analysis of structured materials with desired mechanical properties has become a popular topic in the computer graphics community. Bickel et al. [2010] designed, printed, and measured such materials, and used a combinatorial approach to combine structures to create a desired deformation behavior. Avoiding the manual design and measurement step, Schumacher et al. [2015] and Panetta et al. [2017; 2015] used numerical simulation to predict the macroscopic behavior of individual microstructures, and described optimization-driven solutions to fill objects with microstructure cells in order to achieve desired spatially-varying material behavior. Martinez et al. [2016] employed

an efficient stochastic approach to create isotropic Voronoi foams and orthotropic foams [Martínez et al. 2017] and determined the mapping between structure parameters and mechanical properties.

Pérez et al. [2015] presented an approach to create light-weight and cost-effective rod meshes—which cannot be classified with bulk properties—with a desired deformation behavior and later combined two different material domains by printing rod structures directly on a pre-stretched cloth to create curved surfaces [Pérez et al. 2017]. Connecting the advantages of silicone with the expressiveness of structured materials, Zehnder et al. [2017] introduced a material design approach that uses inclusions embedded in silicone to create various material behaviors.

As an extension to purely functional structured materials, several works have explored the design of decorative shell-based structures, combining stability with aesthetic goals during the design process. To create stable, decorative shell structures, Dumas et al. [2015] extended the idea of texture synthesis into the domain of digital fabrication. With a similar goal, Zehnder et al. [2016] introduced a method to create ornamental curve networks using a rod-based parameterization that avoids rasterization and provides a high degree of artistic control. Martinez et al. [2015] described an optimization approach that combines texture synthesis with a topology optimization method to create artistic and stable two-dimensional structures. Schumacher et al. [2016] introduced a similar approach to create structured shells by combining discrete element textures with a shell-based topology optimization method.

In our work, we emphasize the characterization of structured materials and investigate anisotropic and nonlinear material behavior of thin structured sheets. We define our structures using a periodic network of rods, a parametric representation similar to Panetta et al. [2015], but focus on a visually appealing parameterization that also allows us to implement an efficient structure optimization approach.

Capture and Modeling. Accurate material modeling is a crucial part of any simulation with physical applications. Besides formulating an appropriate material model, measuring the material properties can be a challenging task. Bickel et al. [2009] presented a data-driven material model for soft tissue. However, for the purpose of characterizing structured sheets, methods that investigate flat materials—for example cloth—are more suitable. Wang et al. [2011] and Miguel et al. [2012] presented systems to capture the deformation of cloth in various configurations and determine the corresponding material models. Likewise, methods for designing and modifying materials in an intuitive fashion [Li and Barbič 2015; Xu et al. 2015] allow us to determine the material properties that lead to a desired deformation behavior.

The theory of *numerical homogenization* [Hassani and Hinton 1998] provides a way to replace small-scale structures with an averaged, homogeneous material. Such an approach allows for the simulation and characterization of structured materials without the need to use high-resolution models. Kharevych et al. [2009] and Nesme et al. [2009] presented homogenization approaches that approximate a heterogeneous model using a coarse mesh with spatially-varying material properties. Chen et al. used a database of material combinations to create a data-driven finite element method [2015], and

introduced a specialized homogenization approach for dynamic simulations [2017]. Geers et al. [2007] described a nonlinear homogenization approach for thin sheets that uses a full solid simulation to compute the material response on the microscopic level without fitting a material model.

The structures that we focus on in our method can be modeled as networks of elastic rods—a model that has been used to simulate similar structures in [Megaro et al. 2017; Pérez et al. 2015; Zehnder et al. 2016]. We use these rod networks as the high-resolution basis for a homogenization approach, which allows us to capture the macromechanical properties of these networks. Our characterization method is similar to the work of François et al. [2017], who use directional Young’s modulus plots to visualize the material properties of triangular lattices, based on a parameterized analytical model. In contrast, our homogenization-based approach allows us to characterize any type of flat, periodic structure.

Outside of computer graphics, the mechanical engineering and materials science communities have shown significant interest in the design and analysis of structured materials. Such structures can be found as the result of stochastic processes in naturally occurring materials, where they are often modeled as *random fiber networks* [Picu 2011]. For more regular structures, approaches to homogenize truss networks [Hutchinson and Fleck 2006] compute the macroscopic behavior of periodic, *mechanism-like* assemblies. At smaller scales, these structures can also stem from the underlying atomic composition, in the case of crystal structures or graphene sheets [Lu and Huang 2009]. Maybe the most promising application of structured materials is in the domain of *mechanical metamaterials*—materials whose structure is tailored to show desired material properties [Bertoldi et al. 2017]. Metamaterial approaches include unit cell–based combinatorial structures [Coulais et al. 2016], origami- and kirigami-inspired designs [Xu et al. 2017], and the exploitation of mechanical instabilities [Kochmann and Bertoldi 2017]. Auxetic structures have been a focus of interest, with the investigation of bistable auxetic structures [Rafsanjani and Pasini 2016] and auxetic behavior over large ranges of deformations [Liu and Zhang 2018]. However, these approaches generally use hand-picked designs, and run an in-depth analysis on them. While this is useful to fully understand the mechanics of a given structure, it does not lend itself to an intuitive characterization and exploration of a large set of structures.

Polygonal Patterns and Other Tilings. Computer Graphics has traditionally been interested in procedural pattern generation for decorating digital surfaces, both with texture and with geometric structures. Besides architectural applications of meshing and tiling methods [Jiang et al. 2015; Tang et al. 2014], some of these approaches take inspirations from physical pattern creation in quilting [Zhou et al. 2006] or weaving [Akleman et al. 2009]. Others use tilings to create efficient samplings [Ostromoukhov 2007]. In a combination of geometry and fabrication, Konaković et al. [2016] used the unique properties of auxetic mechanical materials to design surfaces that can be fabricated from a single flat piece of material.

Space-filling tilings of the plane offer an interesting parameterization for visually appealing structures, and have been studied

extensively in the mathematics community [Grünbaum and Shephard 1986]. Kaplan and Salesin [2000] used a special class of space-filling tilings, isohedral tilings with curved edges, and in subsequent work in this direction investigated the synthesis of Islamic star patterns [Kaplan and Salesin 2004]. We take inspiration from the aesthetics and the continuous parameterization of these tilings, and investigate the space of mechanical properties that they create.

3 STRUCTURED SHEET MECHANICS

Structured sheets offer a rich space of heterogeneous materials with direction-dependent and nonlinear resistance to membrane and bending deformations. Our goal is to establish a formal but intuitive language for describing the mechanical properties of these materials, and to provide insight in the connection between their structure and mechanics.

In order for this analysis to be meaningful, we must be able to predict the deformation of structured sheets under imposed loads or boundary conditions using simulation (Section 3.2). To investigate their macromechanical behavior, we turn to numerical homogenization (Section 3.4) and condense the mechanics of the heterogeneous networks, simulated at their native mesoscopic level, into the familiar framework of linear elasticity. This process gives rise to elasticity tensors that characterize the direction-dependent stress-strain behavior around a given state of deformation. Since this representation does not readily lend itself to interpretation, we convert these elasticity tensors into radial plots of Young’s modulus, Poisson’s ratio, and bending stiffness (Section 3.5).

3.1 Phenomenology

In order to make an informed decision on the computational models to use in our analysis, we must first determine the salient characteristics that govern the deformation behavior of structured sheet materials. We are particularly interested in how deformations at the native, mesoscopic scale (from 1–5mm) of the material give rise to macroscopic deformation effects (from 5–10cm). To this end, we experimentally investigated the behavior of network structures subjected to different boundary conditions that create in-plane and out-of-plane deformations. We briefly summarize the central qualitative findings here and provide extensive, quantitative analysis in Section 5 and the supplemental material.

Membrane. Structured sheet materials are networks of interconnected rods. When imposing an external deformation onto the network, the individual rods will either stretch, bend, or twist—rods do not compress but buckle out of plane instead. For a given imposed deformation, the ratio between bent and stretched rods is an indicator of the stiffness of the network for that specific deformation. Since the resistance to bending is much smaller than the resistance to stretching, *bending-dominated* networks will be softer than *stretching-dominated* networks. For a given structure, this property, and therefore the overall stiffness, depends on the direction of the imposed deformation.

Beyond a certain maximum deformation, however, all rods will eventually be stretched and the structure will transition into a stiff

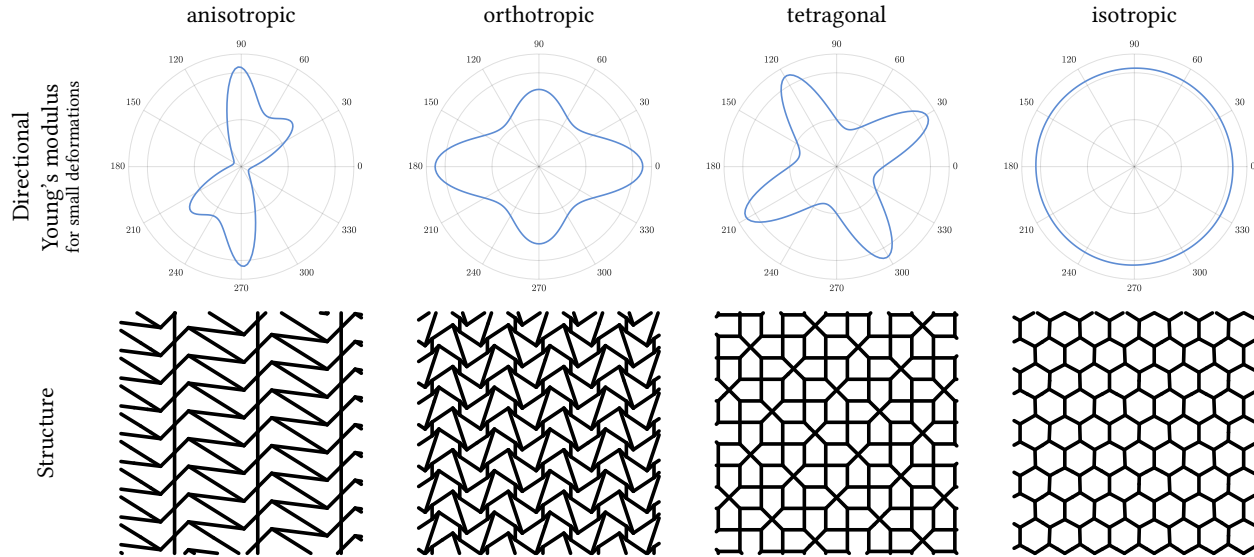


Fig. 2. Two-dimensional linear materials can be classified into four symmetry groups: anisotropic, orthotropic, tetragonal, and isotropic. The various material symmetries lead to characteristic Young's modulus profiles and can be related to the structural symmetries of the underlying tiling.

regime. These two observations indicate that structured sheet materials are characterized by anisotropic and nonlinear in-plane stiffness.

Bending. Similar to their in-plane deformation behavior, the stiffness response of structured sheets to bending is strongly anisotropic, but nonlinearities are generally less pronounced. It is insightful to draw the analogy to the simpler case of thin sheets made of homogeneous material, whose bending resistance depends only on their thickness and the mechanical properties of the bulk material. But unlike sheets made of homogeneous material, and due to the heterogeneity of structured sheets, the correlation between membrane and bending stiffness is only weak, making it necessary to treat bending separately from stretching to capture a complete picture of the mechanical properties.

With their salient characteristics spelled out, we can now proceed to the question of which computational models to use for structured sheets at the mesoscopic and macroscopic scales, respectively.

3.2 Mesoscopic Model

To accurately model the mechanics of our networks at their native mesoscopic scale, their structure needs to be captured in sufficient geometric detail. As a good compromise between accuracy and efficiency, we opt to model structured sheets as networks of thin Kirchhoff rods. Our implementation is based on the discrete elastic rod model [Bergou et al. 2010; Kaldor et al. 2010]. We use the extension to networks described by Zehnder et al. [2016] to model connections with more than two rod segments: we place a rigid body frame at each such connection, and define the bending and twisting energies at the connection not between two neighboring segments, but between a segment and the rigid body frame. The frame is added to the simulation variables, and will rotate to minimize the energy.

The discrete rod model can be applied almost directly to our case, except for one important modification: due to the complex structure of the networks, stretching the material in a given direction will also induce compressions in some rods. In physical reality, these compressions immediately resolve into out-of-plane buckling, but under the perfectly planar and symmetric conditions in simulation, compressions will persist and give rise to unstable equilibrium configurations. Besides the associated numerical difficulties, persistent compressions lead to an overall much stiffer deformation response than what is observed in reality. To avoid such parasitic stiffening, we use a full three-dimensional model even for deformations that are, on the macroscopic level, in-plane, and slightly perturb the initial state into the normal direction, forcing compressions to resolve into bending. Thanks to this modification, the rod model shows very good agreement with physical experiments, both in terms of force-deformation behavior and local deformations observed in the structures; see Section 5.1.

3.3 Macroscopic Model

On the macroscopic level, the most salient characteristic of structured sheets is arguably their direction-dependent stiffness response to stretching and bending deformation. Together with their thin nature and planar rest state, this deformation behavior suggests a macromechanical model based on the theory of anisotropic Kirchhoff plates (see, e.g., [Hwu 2010, Section 1.4]), which postulates a strain energy density of the form

$$W(\boldsymbol{\epsilon}, \boldsymbol{\kappa}) = \frac{1}{2} \boldsymbol{\epsilon} : \mathbb{C} : \boldsymbol{\epsilon} + \frac{1}{2} \boldsymbol{\kappa} : \mathbb{B} : \boldsymbol{\kappa} = W^M + W^B, \quad (1)$$

where $\boldsymbol{\epsilon}$, $\boldsymbol{\kappa}$ are membrane and bending strains, respectively, and \mathbb{C} , \mathbb{B} are corresponding material stiffness tensors. The strains and stresses are rank-2 tensors that can be represented as symmetric 2×2 -matrices; \mathbb{C} and \mathbb{B} are symmetric rank-4 tensors with 16 entries. Due

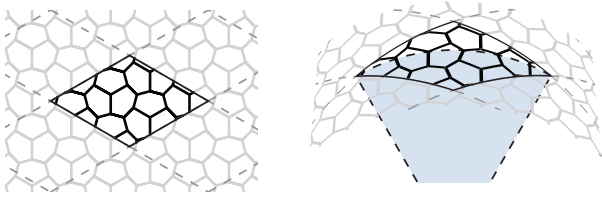


Fig. 3. Periodic boundary conditions for in-plane deformations emulate a flat tiling of patches (left). For curved configurations, the tiling is mapped to a cylinder, where adjacent patches are related through a rotation and translation (right). Additional details can be found in Appendix A.

to their symmetry, only 6 entries can be independent, even in the case of complete anisotropy. Differentiating the energy density with respect to membrane and bending strains gives rise to membrane and bending stresses,

$$\begin{aligned}\sigma &= \mathbb{C} : \epsilon \\ \mathbf{M} &= \mathbb{B} : \boldsymbol{\kappa}.\end{aligned}\quad (2)$$

The above expressions underline the linear nature of this material model—we will describe extensions to account for nonlinearities in Section 3.4—and the decoupling of the membrane and bending energies. While this model only approximates the full nonlinear material behavior, it is sufficient to capture the salient material properties that we are interested in.

With the mesoscopic and macromechanical models defined, we can now proceed to the mapping between the two via homogenization.

3.4 Homogenization

The essential idea of homogenization is to subject a tileable *unit cell* of material to various boundary conditions that create different states of deformation. These boundary conditions have to preserve tileability on the mesoscopic scale while at the same time leading to deformations that are easily quantified on the macroscopic scale. Figure 3 shows the general concept of these boundary conditions: for flat configurations, they emulate a tiling of a single patch of the structure in the plane, while curved configurations are possible if we introduce a rotational component to the tiling. We refer to Appendix A for a detailed description of the boundary conditions used for membrane and bending experiments. When using these periodic boundary conditions, special care has to be taken to ensure that the simulated structure is not too small to capture all deformation properties of the full structure. Specifically, the buckling modes of a structure can often extend over two of the smallest tileable unit cells. To capture these buckling modes properly, we always apply our homogenization on a 2×2 patch of the smallest tileable unit cells.

While classic plate theories generally establish a shared set of parameters that connect the membrane and bending behavior—both are fully described by a single Young’s modulus and Poisson’s ratio in the case of a homogeneous isotropic plate—this connection has been found to disappear in structured materials [O’Donnell and Langer 1962]. Having confirmed these findings in our own

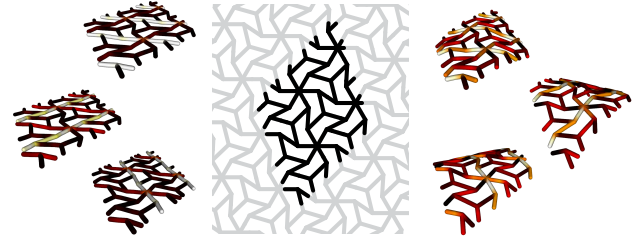


Fig. 4. Example deformations obtained by applying different loads to the boundary of a periodic patch of a structure. Left: membrane deformations corresponding to uniaxial stretching. Right: bending deformations corresponding to uniaxial (or cylindrical) curvature.

physical experiments, we perform homogenization independently for membrane and bending properties.

Membrane Material Tensor Fitting. Given a structured sheet material, we seek to find elasticity parameters for the macroscopic model that best approximate the true stress-strain behavior of the mesoscopic model. To this end, we must first determine a set of *test deformations* and corresponding boundary conditions that will be used to probe the material in simulation. For the membrane part, a natural choice are uniaxial tension states, for which the strain in a specific direction is prescribed while the perpendicular direction is only subject to periodic boundary conditions (see Figure 4). Uniaxial deformations generally describe the material behavior sufficiently well, but we found that some structures require more information to fit a macroscopic material tensor. Whenever such a case is detected (from the rank of the fitting matrix), we augment the test set with an additional biaxial deformation that prescribes a uniform stretch in all directions.

Once the set of test deformations is defined, we perform meso-scale simulations and compute the macroscopic strains and stresses using the approach described in Appendix B. The resulting set of N stress-strain pairs are then used to fit a homogenized *compliance tensor* in a least squares sense,

$$\mathbb{S}^H = \arg \min_{\mathbb{S}} \sum_{i=1}^N \frac{1}{\|\epsilon_i\|_F^2} \|\mathbb{S} : \sigma_i - \epsilon_i\|_F^2, \quad (3)$$

where ϵ_i and σ_i are the strain and stress of the i -th test deformation, respectively, and $\|\cdot\|_F$ is the Frobenius norm. The solution to Equation (3) is a homogenized material compliance tensor \mathbb{S}^H , and the corresponding homogenized material stiffness tensor can be computed through the symmetric inverse, $\mathbb{C}^H = (\mathbb{S}^H)^{-1}$. One could also fit the homogenized material stiffness tensor \mathbb{C}^H directly; however, we found that since the significant anisotropy of certain structures leads to extreme stresses, measuring error in strain space leads to improved robustness.

Bending Material Tensor Fitting. The bending behavior of a material is characterized by its bending moment response to applied curvatures. Similar to the in-plane stiffness, we design a set of test deformations that fully describe this behavior. Cylindrical bending is a natural choice for this purpose, since this type of deformation does not induce Gaussian curvature and hence minimizes interference

with membrane deformations. Cylindrical bending alone, however, is not sufficient to uniquely determine the bending stiffness tensor, as is apparent by the rank-deficiency of the fitting matrix. We therefore account for the missing data by augmenting the cylindrical test deformations by a single deformation with spherical curvature. For each of the M boundary conditions in the resulting test set, we then perform meso-scale simulations to obtain the corresponding deformed network.

While the direct analogy to the membrane case would be to compute macroscopic bending moments for the deformed networks, the curved patch boundaries complicate the direct computation of moments. We therefore use the energy density of the deformed patch in order to fit the homogenized bending stiffness

$$\mathbb{B}^H = \arg \min_{\mathbb{B}} \sum_{i=1}^M \left(\frac{1}{2} \boldsymbol{\kappa}_i : \mathbb{B} : \boldsymbol{\kappa}_i - W_i \right)^2, \quad (4)$$

where $\boldsymbol{\kappa}_i$ and W_i are the prescribed curvature tensor and energy density for the i -th test deformation, respectively.

Determining the Test Set. The set of deformations that are used to fit the stiffness tensors influence the quality of the result. While a set of only three deformations is sufficient to fit the tensor for infinitesimal strains, the nonlinearities that appear for finite strains require that we choose a suitable set of deformations that captures the material properties in sufficient detail and will reproduce the global deformation behavior in the fitted material tensor. We found that for most structures, a small number of up to 20 deformations is sufficient for a robust fitting to a linear material tensor. For highly anisotropic and nonlinear materials, however, a larger number of deformations generally leads to improved fitting results. To this end, we use a cross-validation scheme that adaptively determines the number of test deformations needed to obtain robust homogenization results. From a given set of N test deformations, we use multiple sets of 80% as training data to fit a stiffness tensor, then measure its performance on the remaining 20% of the test set. If the error on the test data is larger than on the training data, we increase the number of test deformations to $2N$ and repeat the process.

Nonlinearities. The homogenized stiffness tensors provide a linearized description of a material's direction-dependent stress response. For a given structure, the result of the fitting process is influenced by two factors: the reference state of deformation for which the tensor is computed, and the magnitude of the imposed deformation away from the reference state. The choice of reference state, not to be confused with the rest state, is important when there is nonlinear coupling between deformation modes. In principle, a comprehensive description of the nonlinear material behavior can be obtained by densely sampling the deformation space. However, besides the computational complexity of such an approach, the massive amount of high-dimensional data points generated in this way would simply be overwhelming for the user. We argue that, for the purpose of understanding and navigating the space of materials, conciseness is far more important than completeness. In order to convey a compact description of a material's direction-dependent nonlinearity, we simply create multiple test sets with uni- and biaxial deformations of varying magnitude (0.1% and 10.0%) and

curvature (0.1m^{-1} and 5m^{-1}) around the rest state. Taken together, the corresponding stiffness tensors fitted to these different test sets can then be condensed into a concise and intuitive description of nonlinear, direction-dependent material behavior as described next.

3.5 Representing Direction-Dependent Elasticity

Although the stiffness tensors provide a full picture of the material behavior around a given state of deformation, their entries are rarely used to describe a material: they are hard to correlate to quantities that can be measured directly and, consequently, provide little intuition about the material behavior. In the following, we describe how to distill these stiffness tensors into representations that lend themselves more readily to interpretation. We will briefly introduce the formulas to extract these representations from the stiffness tensors, but refer to the supplemental document for a more in-depth explanation.

Membrane. An intuitive set of measures for the membrane behavior are the *Young's modulus* E , describing the force per area required to stretch the material to one unit of deformation, and the *Poisson's ratio* ν , which is the amount of transverse contraction for a unit extensional deformation. Taken together, Young's modulus and Poisson's ratio completely characterize the behavior of linear isotropic materials. By allowing E and ν to vary depending on the direction \mathbf{d} , they can also be used to describe anisotropic materials.

In order to derive direction-dependent expressions for E and ν , we use the the compliance tensor $\mathbb{S} = \mathbb{C}^{-1}$. This tensor allows us to compute the deformation induced by the uniaxial unit stress $\boldsymbol{\sigma}^{\mathbf{d}} = \mathbf{d}\mathbf{d}^T$, which is the configuration in which the two material properties are measured. The directional Young's modulus can then be computed as

$$E(\mathbf{d}) = \frac{1}{(\mathbf{d}\mathbf{d}^T) : \mathbb{S} : (\mathbf{d}\mathbf{d}^T)}. \quad (5)$$

Similarly, we compute the directional Poisson's ratio, describing the relative compression of the material along the direction \mathbf{n} perpendicular to the stretch direction \mathbf{d} , as

$$\nu(\mathbf{d}) = -\frac{(\mathbf{d}\mathbf{d}^T) : \mathbb{S} : (\mathbf{n}\mathbf{n}^T)}{(\mathbf{d}\mathbf{d}^T) : \mathbb{S} : (\mathbf{d}\mathbf{d}^T)}. \quad (6)$$

Bending. We can follow a similar approach for the characterization of the bending behavior of a structured sheet material. However, we found that the Young's modulus equivalent of the bending stiffness matrix, which is measured by applying a uniaxial bending moment to the structure, describes a state that is hard to reproduce in a real application, since it will automatically cause in-plane deformations that generally dominate the deformation mode. Instead, we characterize the bending behavior of the material using a natural low energy state of purely cylindrical curvature, or zero Gaussian curvature. Given a direction \mathbf{d} , we compute the directional bending moment generated by a unit curvature,

$$b(\mathbf{d}) = (\mathbf{d}\mathbf{d}^T) : \mathbb{B} : (\mathbf{d}\mathbf{d}^T). \quad (7)$$

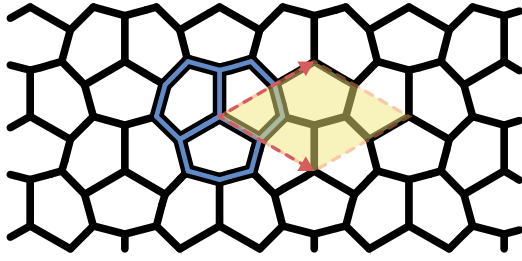


Fig. 5. The translational unit (blue) of an isohedral tiling creates an infinite periodic tiling of the plane using only translations (red). The translation vectors define the minimal tileable unit cell (yellow) necessary for a simulation with periodic boundary conditions.

4 TILINGS AND SYMMETRIES

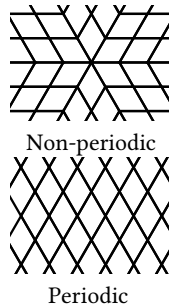
Apart from periodicity constraints, the machinery introduced so far makes no assumptions on the nature of the patterns. To investigate the interplay between structure and mechanics, we will from now on focus on the class of isohedral tilings, which we briefly introduce below. We pay special attention to the symmetry properties of the patterns and how they relate to symmetries in the material behavior.

4.1 Isohedral Tilings

Isohedral tilings are a special class of mono-hedral tilings—tessellations built from a single base tile—in which only tiles transformed under the symmetry group of the tiling are allowed. In practical terms, this means that an isohedral tiling has translational periodicity (see inset figure).

From a combinatorial point of view, 93 different families of isohedral tilings can be identified [Kaplan 2009], referred to individually as IH01 to IH93. Each family has a polygonal base tile ranging from a triangle to a hexagon, with a parameterization having zero to six degrees of freedom. Up to 12 base tiles then form a *translational unit*, the smallest structure of a family that can be tiled infinitely by only applying translations (see Figure 5). For our structures, we create a consistent scale between families by normalizing the area of the translational unit.

Symmetries. Isohedral tilings exhibit a high degree of visual regularity that can be quantified in terms of symmetries. Intuitively, the individual translational units of an isohedral tiling span a hexagonal or parallelogrammatic grid. Such a grid, and therefore the tiling, may have twofold, threefold, fourfold or sixfold rotational symmetry. Similarly, isohedral tilings can have glide reflection symmetries—a combination of reflection and translation along the reflection axis—along one, two, three, four, or six reflection axes. We can observe all of these rotational symmetries in our isohedral tilings, and, as it turns out, these are also the only rotational and reflectional symmetries that isohedral tilings can have [Grünbaum and Shephard 1986].



Besides their visual impact, geometric symmetries in the tiling also induce symmetries in the material behavior. In order to investigate the nature of this relation, we first review material symmetries below.

4.2 Material Symmetries

The mechanical properties of a material can exhibit various symmetries. For example, any two-dimensional material rotated by 180° will still show the same material properties. Additional symmetries allow us to define different *symmetry classes* for materials that characterize their qualitative behavior. For a two-dimensional linear material model, there are four distinct symmetry classes: isotropic, tetragonal, orthotropic, and (fully) anisotropic materials.¹ See Figure 2 for example structures from these categories and their corresponding Young's modulus profiles. Rather than determining the symmetry class through visual inspection of the Young's modulus profiles, it can be identified from a set of five invariants of the material stiffness tensor \mathbb{C} that measure the various rotation-invariant non-symmetries of the tensor [de Saxcé and Vallée 2013].

Anisotropic materials are the most general symmetry class and do not possess any additional symmetries.

Orthotropic materials have distinct material properties along two orthogonal directions, which introduces a reflection symmetry along these two axes. This symmetry is apparent in the directional Young's modulus plot of a material, where two axes that show a local maximum or minimum are perpendicular to each other.

Tetragonal materials are special types of orthotropic materials whose material properties along any pair of orthogonal directions are identical, making them invariant to rotations of 90° , and giving them a total of four equally-spaced axes of reflection. Due to the rotational symmetry, tetragonal materials are easily identifiable from their Young's modulus plot.

Isotropic materials are the most constrained type of elastic material. They show a direction-independent material behavior, and are therefore invariant under any rotation or reflection. On a Young's modulus plot, isotropic materials can be easily identified as circles.

4.3 Shared Symmetries

We can now investigate the connection between the symmetries of the material properties and the geometric symmetries of our structured sheet materials, and we summarize the mapping between the symmetries in Table 6. Note that this mapping is one-way—while the geometry of the structure dictates the necessary material symmetries, a specific material symmetry does not require any geometric symmetry. Figure 12 shows an example of a structure that is isotropic, but does not possess the geometric symmetries that imply this material symmetry.

The most important factor when comparing geometric symmetries to material symmetries is the inherent rotational symmetry of the material properties: every material property is invariant to rotations of 180° . Tilings with a twofold rotational symmetry will therefore not add any new symmetries to the material properties,

¹Unless specifically noted, we use the name of a symmetry class to refer to patterns that have that symmetry but not any greater symmetry; for example *orthotropic* means the material is orthotropic but not tetragonal or isotropic.





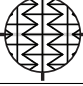

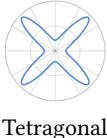


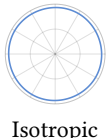



Geometric symmetry			Material symmetry
	Twofold rotation	⇒	 Anisotropic
	One-axis reflection	⇒	 Orthotropic
	Two-axis reflection		
	Fourfold rotation	⇒	 Tetragonal
	Four-axis reflection		
	Threefold rotation	⇒	 Isotropic
	Sixfold rotation		
	Three-axis reflection		
	Six-axis reflection		

Fig. 6. The different symmetry classes for isohedral tilings (left) and the corresponding material symmetries that they induce (right).

and in general, the material symmetry will be a combination of the geometric symmetry and a 180° rotation. A special case are structures with threefold and sixfold geometric symmetries, and three-axis and six-axis geometric glide reflection symmetries, which all show the same material response along at least three axes, or six directions. In the case of a linear material, these responses provide a complete basis of the underlying space, and since all responses are rotationally symmetric, every other response must also be rotationally symmetric, making the material *isotropic*.

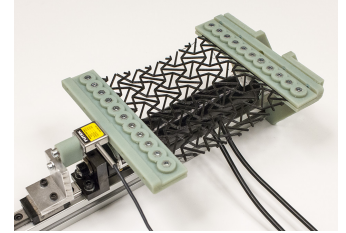
5 RESULTS

We used our method to characterize a large number of structures from the space of isohedral tilings and present our findings in this section. We first start with general observations, then highlight specific properties on selected examples. Finally, we present extensions to (inverse) material design to create tilings with desired deformation behavior.

But first, we will show a validation of the rod model introduced for the mesoscopic simulation in Section 3.2.

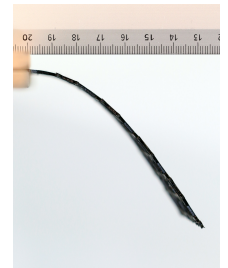
5.1 Mechanical Testing

We validated our simulation model on a set of tension and bending tests, using the structures shown in Figure 7. The structures were printed as patches of $100\text{mm} \times 100\text{mm} \times 1.2\text{mm}$ on an Ultimaker 2 printer with a Flex3Drive extruder, using the rubber-like



NinjaFlex material. The tensile testing setup, shown in the inset figure, uses a linear actuator and a load cell to perform uniaxial tension tests, automatically capturing reaction forces of samples under tensile loads. We measured the Young's modulus of the base material to be 15.5 MPa, based on a tensile test of a *dogbone* (tensile specimen), and determined a Poisson's ratio of 0.48 based on standard values for TPU materials [Qi and Boyce 2005]. Using these values in simulation leads to results consistent with the experimental data for a large range of structures (see Figure 8).

Since the bending stiffness of structured sheets is significantly lower than its in-plane stiffness, the self-weight of the material needs to be accounted for during measurements. We therefore opted to follow Pabst et al. [2008] and Miguel et al. [2013], measuring the curvature-moment curves of our samples using the gravity-assisted method of Clapp et al. [1990], which uses visual data and polynomial fitting to extract



material parameters from a specimen (see inset). We use this method on both the printed and simulated structures. Figure 9 shows an overview of the resulting bending stiffnesses for small curvatures, the full results can be found in the supplemental material. As can be seen from the data, the deviation between measurements and simulations is larger for the bending tests than for the tensile tests. We speculate that this difference is largely due to the inaccuracies of the visual capture approach and the increased uncertainty of the fabrication process along the height dimension.

5.2 Space of Structures

Applying our mechanical characterization approach to many structures from the space of isohedral tilings reveals the *gamut* of mechanical properties that they cover. The visualization of this gamut is, however, not a trivial task. Figure 10 shows a plot of the minimal and maximal directional Young's moduli of all isohedral tiling families, using a regular sampling of the tiling parameters in the interval $[-1, 2]$ resulting in around 5500 valid structures. We used the material parameters presented in Section 5.1 on patches with an area of 16cm^2 , a rod diameter of 1.5mm^2 , and a maximum segment length of 2.5mm^2 . The data shows that our sampling covers a directional Young's modulus range of roughly five orders of magnitude, with the minimal directional Young's modulus of a structure

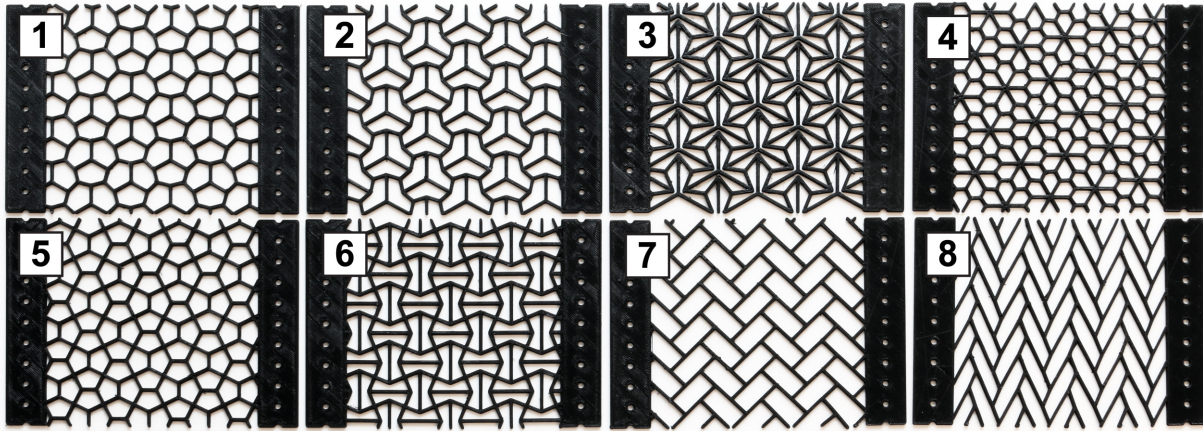


Fig. 7. The structures used in the experimental validation and for the characterization in Figure 11, covering a wide range of visual styles and mechanical properties. Structures 1 to 3 are part of the IH07 family, structure 4 is from IH21, structures 5 and 6 from IH29, and structures 7 and 8 are part of IH02.

covering four orders of magnitude, and the maximal directional Young's modulus covering three orders of magnitude. The bending stiffness shows a smaller variation, covering a range of two orders of magnitude. While this visualization is useful to determine the practical boundaries of Young's moduli we can expect from these structures, it does not lend itself to exploration, and only shows a limited view of the mechanical properties.

A proper exploration of mechanical properties of such a space is best done interactively. We therefore organized our dataset into an interactive material browser (www.structuredsheets.com). It offers visualization of various mechanical properties for the whole dataset or individual families, as well as a detailed mechanical characterization and visualization of individual structures. Note that some of the 93 families of isohedral tilings are subsets of other families, and were excluded from the dataset.

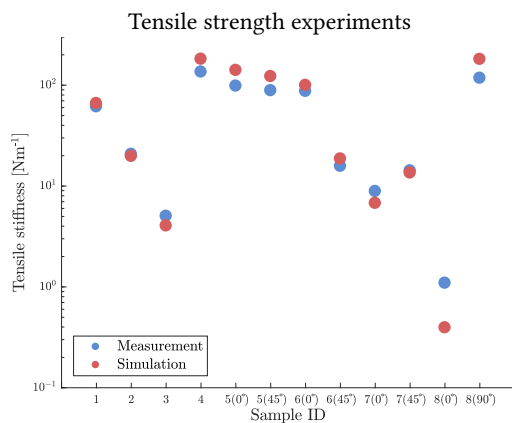


Fig. 8. The tensile stiffnesses measured in our tension experiments (blue), compared to our simulation results (red), at 10% strain. The full measurements can be found in the supplemental material.

Change of Rod Parameters and Dimensions. The results of the mechanical characterization of isohedral tilings are specific to the rod parameters that we determined in Section 5.1. While the differences in geometry of the individual structures allow us to navigate within the gamut of mechanical properties, these rod parameters allow us to modify the gamut itself. The underlying mesoscopic simulation model directly specifies the parameters that influence the characterization, and therefore this gamut: the Young's modulus and Poisson's ratio of the base material, the cross sectional area of the rods, and the size of a single patch of the tiling.

The Young's modulus appears as a linear factor in the formulation of the rod energy, and allowing us to linearly scale the mechanical properties connected to the stiffness, i.e., Young's modulus and bending stiffness.

The Poisson's ratio of the base material is only used in the twisting energy of the mesoscopic simulation. Since twisting has a negligible effect on the mechanical in-plane behavior in the structures we

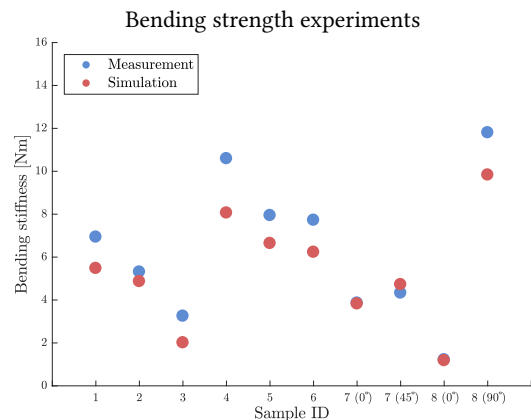


Fig. 9. The bending stiffness measured in our bending experiments (blue), compared to our simulation results (red), at 20m^{-1} curvature. The full measurements can be found in the supplemental material.

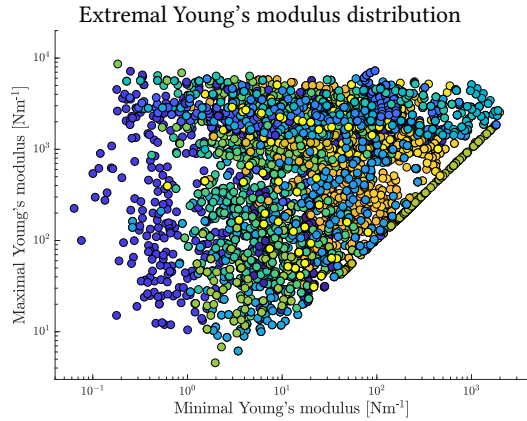


Fig. 10. The gamut of directional Young's moduli covered by isohedral tilings, plotted as the minimal and maximal directional Young's modulus of each structure of our sampling. The colors of the data points represent the isohedral tiling family the structure belongs to.

investigated, the membrane characterization is largely independent of the Poisson's ratio. The bending behavior, on the other hand, can show significant twisting of rods. Since a rod's resistance to twisting will increase with lower Poisson's ratio, the whole gamut of macroscopic bending stiffness will shift towards higher values if we decrease this parameter.

Finally, the cross sectional area and patch area are linked quantities. If we keep their ratio, but scale them, the material properties will scale by the same amount. Interesting effects emerge when this ratio changes, and we can investigate this effect by keeping the patch size fixed and increasing the rod diameter: the mesoscopic simulation model tells us that the stretch energy part of the rod model will scale linearly with the cross sectional area, while the bending and twisting energies scale quadratically. The change in elastic response of a structure then lies within these bounds, and the actual scaling depends on whether the structure is bending-dominated or stretching-dominated: for bending-dominated structures, it will be close to quadratic, while for stretching-dominated structures, it will be close to linear.

Since stretching-dominated structures create the stiffest elastic response, and bending-dominated structures are generally softer, this scaling effectively shrinks the gamut of properties if we increase the rod cross section. Additionally, the difference in scaling leads to a decrease in buckling and out-of-plane bending in the structures. Accordingly, a decrease in cross section has the opposite effect: it increases the gamut of material properties, and encourages more buckling and out-of-plane bending.

5.3 Analysis of Individual Structures

We now highlight a number of interesting properties on individual structures. In Figure 11, we present an extensive analysis of the eight structures already used in the validation of the simulation, shown in Figure 7. We chose structures from four different families (IH02, IH07, IH21, and IH29), showing the potential differences in material properties between structures from the same family and

across different families. For each structure, we plot the directional Young's modulus, Poisson's ratio, and bending stiffness computed from the homogenized stiffness tensors, at two different strain magnitudes (0.1% and 10%) or curvatures (0.1m^{-1} and 5m^{-1}) to show the nonlinearity of the material properties. Besides these homogenized values, we also show the ground truth simulation data, i.e., the values extracted from the same type of uniaxial or cylindrical simulation used in the homogenization. We extract the Young's modulus E and Poisson's ratio ν along a direction \mathbf{d} from the simulation with uniaxial stretch along \mathbf{d} as $E(\mathbf{d}) = \mathbf{d}^T \boldsymbol{\sigma}_{macro} \mathbf{d}$ and $\nu(\mathbf{d}) = \mathbf{n}^T \boldsymbol{\epsilon}_{macro} \mathbf{n}$, where we use the macroscopic strain $\boldsymbol{\epsilon}_{macro}$ and stress $\boldsymbol{\sigma}_{macro}$ described in Appendix B, and the direction \mathbf{n} normal to \mathbf{d} . The directional bending stiffness is computed as the energy density divided by the squared curvature.

Isotropy & Anisotropy. Structures 1 to 4 in Figure 11 show a very good fit for an isotropic material behavior for small strains, predicted by their three-fold rotational symmetry (see Section 4.2). The variations in Young's moduli between the structures are large, and especially structures 1 to 3 demonstrate that even for a single family, we can expect significant variations in the elastic responses.

The remaining structures display different types of anisotropic material behavior. Structures 5 and 6, which belong to the same family, show orthotropic material properties. The directional Young's moduli of structure 6 vary by an order of magnitude depending on the direction, and its Poisson's ratio switches from positive to negative for stretching along the main axes.

Structures 7 and 8, which also belong to the same family, show a transition from a tetragonal material to an orthotropic material whose Young's modulus along the horizontal direction is two orders of magnitude smaller than along the vertical direction. This change can be explained by the structure transitioning from a bending-dominated elastic response to a stretching-dominated elastic response along the vertical axis, creating a stiffer mechanical response. Conversely, the response along the horizontal axis becomes more bending-dominated for structure 8, making it softer.

The bending-dominated or stretching-dominated nature of the elastic response plays an important role in the mechanical properties of these structures. For example, structure 1 and 5 are visually similar, but the directional Young's modulus of structure 5 is up to three times higher. This stems purely from the fact that the geometry of structure 5 contains straighter paths, creating a more stretching-dominated response along these directions.

Nonlinearity. The transition from a bending-dominated deformation to a stretching-dominated deformation can not only be observed when we change the geometry of a structure, but also if we increase the strain on a structure. Indeed, most nonlinear effects we can observe in the structures are due to this transition. For example, when the zigzag pattern in structure 8 in Figure 11 unfolds, the induced stretch creates a significantly stiffer elastic response. An analogy can be drawn to the *stiffness percolation* in random materials (see, e.g., [Wilhelm and Frey 2003]), i.e., the point at which a material forms a path that is aligned with a deformation, significantly increasing its stiffness.

Structures 1, 2 and 4 all exhibit stiffness percolation, shown by the increase in stiffness for larger strains. Additionally, while they show

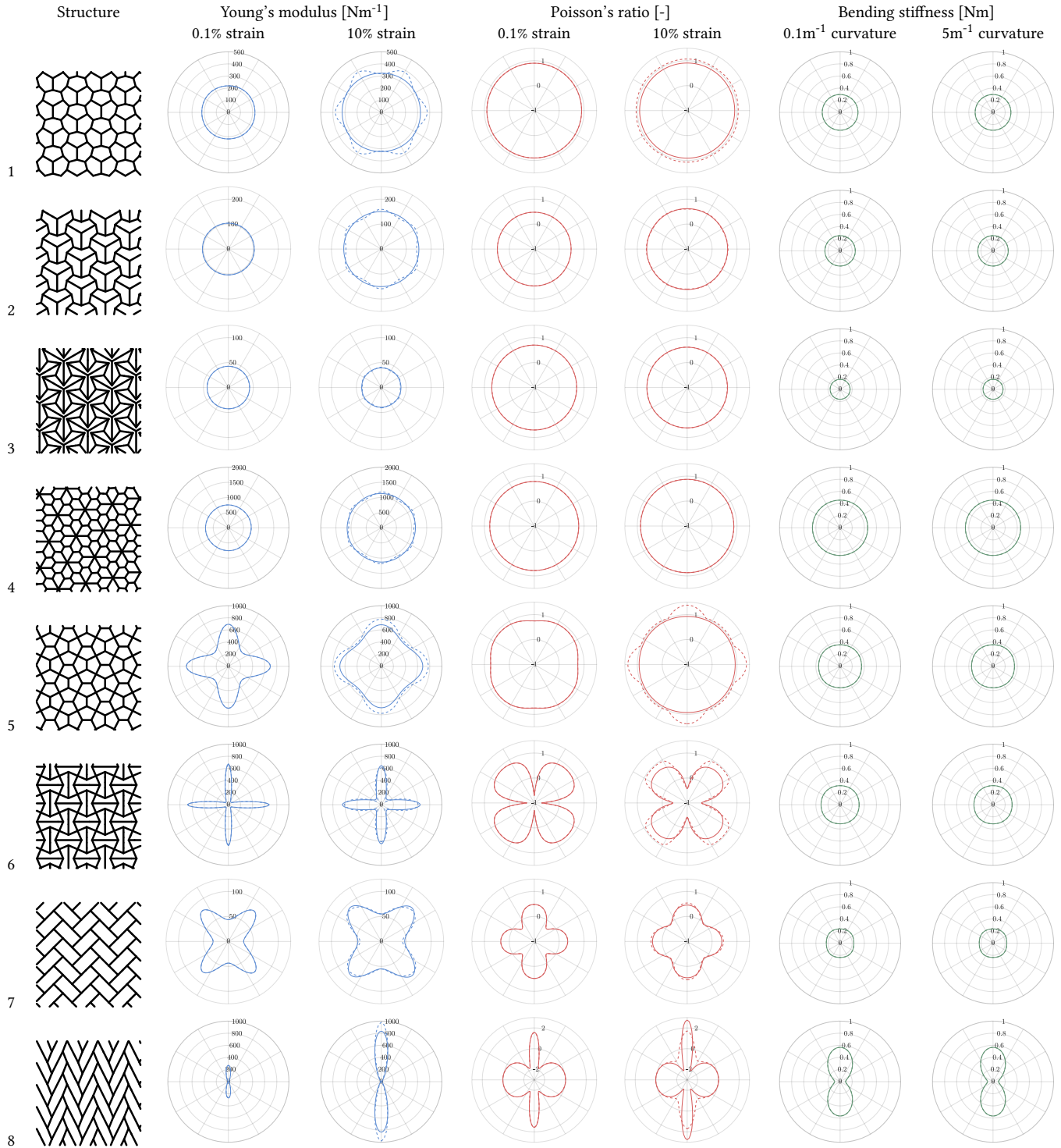


Fig. 11. Simulation results for all structures listed in Figure 7. We show the directional Young's modulus and Poisson's ratio at 0.1% and 10% strain, visualizing the homogenized result (solid line) as well as the simulated value (dashed line). The last two columns show the directional bending stiffness for a curvature of 0.1m^{-1} and 5m^{-1} . Only for larger strains is there a difference between the homogenized result and the full simulation.

an isotropic behavior for small strains, they develop an increasingly anisotropic material response for larger strains, indicated by the six bumps in the directional Young's modulus that align with the symmetry directions of the structure. While the linear approximation cannot capture this anisotropy, it still achieves a good fit for the average Young's modulus.

A different type of nonlinear effect can be observed in structure 3. While it shows the same transition to an anisotropic material response as structures 1, 2 and 4, the average stiffness decreases slightly for larger strains. This decrease can be attributed to the out-of-plane deformations that the structure experiences, allowing it to avoid stiffness percolation for the applied strains. See the accompanying video for a demonstration of this effect.

Bending. The bending response of our structures shows less pronounced anisotropic behavior than their membrane resistance. Even for structure 8, whose Young's moduli span two orders of magnitude, the ratio between the stiffest and softest bending direction is around 5. Additionally, the bending does not exhibit any stiffness percolation, making the bending response more linear, with little change in stiffness between different curvatures.

5.4 Structure Optimization

So far, we have set structure parameters and observed the mechanical behavior that they induce. A natural extension to this forward exploration is to search for structure parameters that lead to desired mechanical properties. As a proof-of-concept that for such an inverse design approach, we optimize for the directional Young's modulus of structured sheets.

Objective. We define an objective based on Eq. (5) by measuring the difference in the directional Young's modulus of our structure and a target function. The directional Young's modulus $E(\mathbf{d})$ is sampled along a set of n directions $\mathbf{d}(\phi_i)$ with equidistant angles ϕ_i between 0 and π . Using the structure parameters \mathbf{p} and an additional rotation parameter α as variables, the optimization objective then becomes

$$O(\mathbf{p}, \alpha) = \frac{1}{2n} \sum_{i=1}^n \left(\frac{E(\mathbf{d}(\phi_i); \mathbf{p}, \alpha)}{E_{goal}(\mathbf{d}(\phi_i))} - 1 \right)^2. \quad (8)$$

Optimization. A simple gradient-based optimization approach is already sufficient to create structures with desired elasticity profiles. We opt for a gradient descent approach with basic backtracking line search. While the derivative of a homogenized material stiffness tensor with respect to the structure parameters can be computed from a series of chain rules, the small number of structure parameters (up to six) allows for an efficient computation of the derivative through finite differences.

Figure 12 shows the result of optimizing for the isotropy of a structure. Given an initial pattern and a target Young's modulus, the optimization finds a similar structure with isotropic material behavior, even though the isotropy cannot be inferred from the geometric symmetries.

We improve our inverse design approach by running multiple optimizations with different starting points, chosen from our dataset with around 5500 structures. This allows us to discard undesired

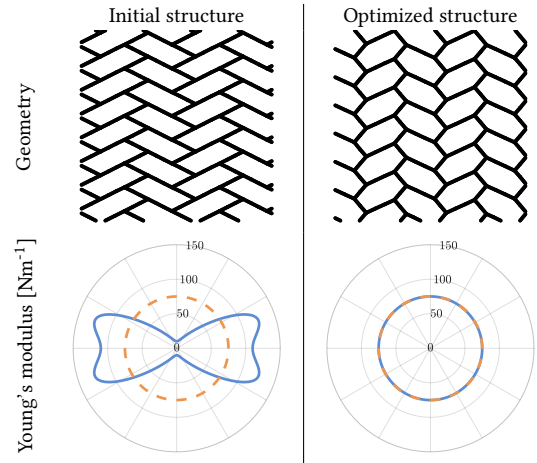


Fig. 12. Starting from a structure from IH09 (top left) with an orthotropic material behavior (blue, bottom left), and a desired isotropic target material behavior (orange), our structure optimization is able to find a similar structure (top right) with the desired material behavior (bottom right).

local minima, and gives us the possibility to provide several results with similar behavior but (potentially) different aesthetics for the user to choose from; see examples shown in Figure 13.

Target Specification. While our optimization approach handles arbitrary Young's modulus targets, defining a physically meaningful Young's modulus distribution without any feedback is a difficult task. We help users by letting them draw a set of points onto the Young's modulus profile and then fit a material compliance tensor \mathbb{S}^{goal} to those points. The fitting uses a linear least squares approach based on Eq. (5):

$$\mathbb{S}^{goal} = \arg \min_{\mathbb{S}} \sum_i \left(E_i((\mathbf{d}_i \mathbf{d}_i^T) : \mathbb{S} : (\mathbf{d}_i \mathbf{d}_i^T)) - 1 \right)^2 \quad (9)$$

for a set of goal directions \mathbf{d}_i and directional Young's moduli E_i .

Optimization Results. Figure 13 shows an optimization result for a target Young's modulus profile corresponding to an orthotropic material. While the initial structures selected from the dataset already match the target fairly well, the optimization can significantly improve on this initial match. Figure 14 shows results for an anisotropic target profile. Here, the initial structures are much further from an optimal result. Nonetheless, our optimization finds structures with the desired mechanical properties by significantly altering, and rotating, the initial structures.

6 CONCLUSIONS

We presented a method to characterize the mechanical properties of structured sheet materials, providing an intuitive approach to analyze and explore their deformation behavior. Using numerical homogenization, we condense the complex deformation behavior of structured sheets, simulated at their native level, into a macromechanical Kirchoff plate model. Our method thus captures

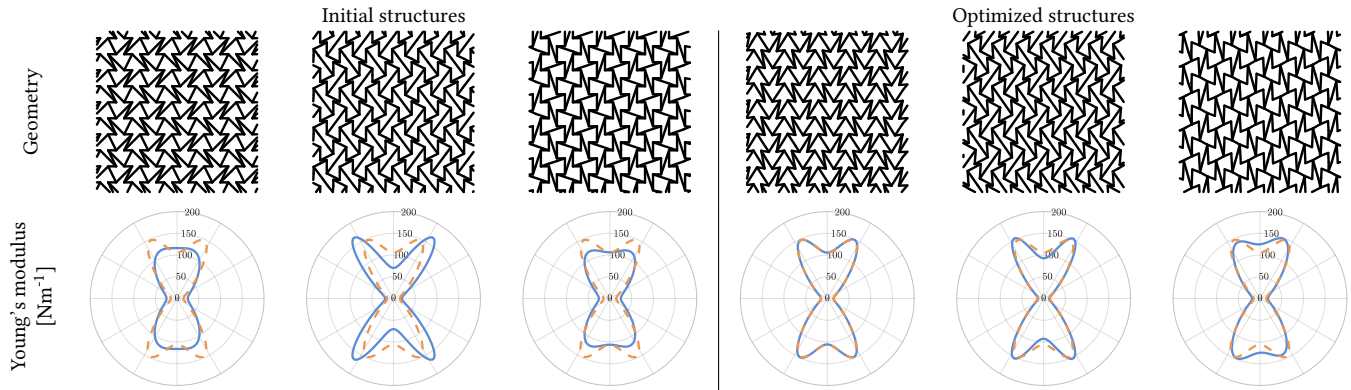


Fig. 13. The results of a structure optimization in the family IH06 for an orthotropic Young's modulus target. The Young's modulus for each initial (left) and optimized structure (right) are shown in blue, along with the target in orange.

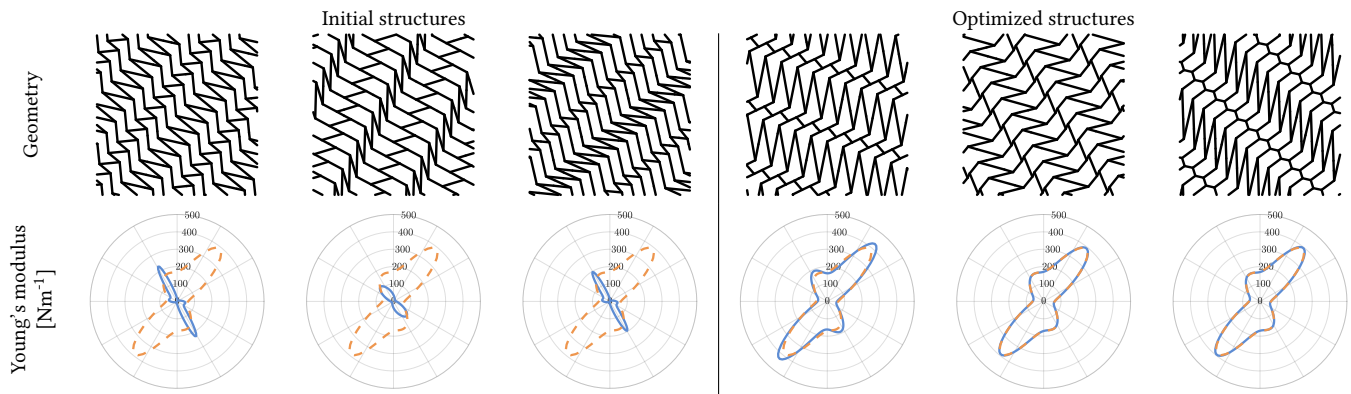


Fig. 14. The results of a structure optimization in the family IH04 for an anisotropic Young's modulus target. The Young's modulus for each initial (left) and optimized structure (right) are shown in blue, along with the target in orange.

the salient mechanical properties of structured sheet materials, including anisotropic stretching and bending resistance as well as nonlinearities for larger strains.

We applied our mechanical characterization method to isohedral tilings, which provide an extensive space of visually pleasing structures with interesting mechanical properties. We investigated the connection between mechanical and geometric symmetries, and determined the conditions which lead to orthotropic, tetragonal, or isotropic materials.

Our method offers an intuitive approach to explore materials, suitable for applications that require a joint design approach that combines aesthetics and material properties. Apart from potential applications in architecture and furniture design, our method might benefit the emerging field of 3D-printed apparel with custom-tailored *look and stretch*.

6.1 Limitations and Future Work

Our current approach characterizes flat structures, but especially for applications in architecture, structured materials with curved rest shapes are of interest. Investigating the influence of rest curvature

on the mechanical properties of the structure might offer insights on how to create optimal synergies between shape and structure.

The linear material model we use for the characterization offers an intuitive way to visualize material properties. However, even though it can also characterize nonlinear material behavior, the model is not accurate for larger strains, and it does not model the interaction between bending and stretching. We consider this trade-off between complexity and conciseness suitable for material characterization, but applications that would use the macromechanical model for simulation and (shape) optimization might require a more accurate and extensive material description.

Many applications of structured materials can benefit from the potential to create *spatially-varying* or *aperiodic* structures, be it for mechanical or purely aesthetic purposes. The required irregular tiling can be created by choosing a specific type of pattern or by relaxing the geometric constraints on isohedral tilings. However, the mechanical characterization of such a tiling is not trivial, and offers many possibilities for future work.

ACKNOWLEDGMENTS

The authors would like to thank Espen Knoop for his help with the testing setup and the voice-over, and Professor Craig S. Kaplan for publishing his isohedral tiling code. The authors would also like to thank the anonymous reviewers for their valuable comments and helpful suggestions.

REFERENCES

- Ergun Akleman, Jianer Chen, Qing Xing, and Jonathan L. Gross. 2009. Cyclic Plain-weaving on Polygonal Mesh Surfaces with Graph Rotation Systems. *ACM Trans. Graph.* 28, 3.
- Miklós Bergou, Basile Audoly, Etienne Vouga, Max Wardetzky, and Eitan Grinspun. 2010. Discrete Viscous Threads. *ACM Trans. Graph.* 29, 4.
- Katia Bertoldi, Vincenzo Vitelli, Johan Christensen, and Martin van Hecke. 2017. Flexible mechanical metamaterials. *Nature Reviews* 2, 17066.
- Bernd Bickel, Moritz Bächer, Miguel A. Otaduy, Hyunho Richard Lee, Hanspeter Pfister, Markus Gross, and Wojciech Matusik. 2010. Design and Fabrication of Materials with Desired Deformation Behavior. *ACM Trans. Graph.* 29, 4.
- Bernd Bickel, Moritz Bächer, Miguel A. Otaduy, Wojciech Matusik, Hanspeter Pfister, and Markus Gross. 2009. Capture and Modeling of Non-linear Heterogeneous Soft Tissue. *ACM Trans. Graph.* 28, 3.
- Desai Chen, David I. W. Levin, Wojciech Matusik, and Danny M. Kaufman. 2017. Dynamics-aware Numerical Coarsening for Fabrication Design. *ACM Trans. Graph.* 36, 4.
- Desai Chen, David I. W. Levin, Shinjiro Sueda, and Wojciech Matusik. 2015. Data-driven Finite Elements for Geometry and Material Design. *ACM Trans. Graph.* 34, 4.
- Timothy G. Clapp, Hong Peng, Tushar K. Ghosh, and Jeffrey W. Eischen. 1990. Indirect measurement of the moment-curvature relationship for fabrics. *Textile Research Journal* 60, 9, 525–533.
- Corentin Coulais, Eial Teomy, Koen de Reus, Yair Shokef, and Martin van Hecke. 2016. Combinatorial design of textured mechanical metamaterials. *Nature*, 529–532.
- Géry de Saxcé and Claude Vallée. 2013. Invariant Measures of the Lack of Symmetry with Respect to the Symmetry Groups of 2D Elasticity Tensors. *Journal of Elasticity* 111, 1, 21–39.
- Jérémié Dumas, An Lu, Sylvain Lefebvre, Jun Wu, and Christian Dick. 2015. By-example Synthesis of Structurally Sound Patterns. *ACM Trans. Graph.* 34, 4.
- Marc L.M. François, Letian Chen, and Michel Coret. 2017. Elasticity and symmetry of triangular lattice materials. *International Journal of Solids and Structures* 129, Supplement C, 18–27.
- Marc G. D. Geers, Erica W. C. Coenen, and Varvara G. Kouznetsova. 2007. Multi-scale computational homogenization of structured thin sheets. *Modelling and Simulation in Materials Science and Engineering* 15, 4, S393–S404.
- Branko Grünbaum and G C Shephard. 1986. *Tilings and Patterns*. W. H. Freeman & Co., New York, NY, USA.
- Behrooz Hassani and Ernest Hinton. 1998. A review of homogenization and topology optimization I-homogenization theory for media with periodic structure. *Computers & Structures* 69, 6, 707–717.
- Robert G. Hutchinson and Norman A. Fleck. 2006. The structural performance of the periodic truss. *Journal of the Mechanics and Physics of Solids* 54, 4, 756–782.
- Chyanbin Hwu. 2010. *Anisotropic Elastic Plates*. Springer US.
- Caigui Jiang, Chengcheng Tang, Amir Vaxman, Peter Wonka, and Helmut Pottmann. 2015. Polyhedral Patterns. *ACM Trans. Graph.* 34, 6.
- Jonathan M. Kaldor, Doug L. James, and Steve Marschner. 2010. Efficient Yarn-based Cloth with Adaptive Contact Linearization. *ACM Trans. Graph.* 29, 4.
- Craig S. Kaplan. 2009. *Introductory Tiling Theory for Computer Graphics*. Morgan & Claypool Publishers.
- Craig S. Kaplan and David H. Salesin. 2000. Escherization. In *Proceedings of the 27th Annual Conference on Computer Graphics and Interactive Techniques (SIGGRAPH '00)*. 499–510.
- Craig S. Kaplan and David H. Salesin. 2004. Islamic Star Patterns in Absolute Geometry. *ACM Trans. Graph.* 23, 2, 97–119.
- Lily Kharevych, Patrick Mullen, Houman Owhadi, and Mathieu Desbrun. 2009. Numerical Coarsening of Inhomogeneous Elastic Materials. *ACM Trans. Graph.* 28, 3.
- Dennis Kochmann and Katia Bertoldi. 2017. Exploiting Microstructural Instabilities in Solids and Structures: From Metamaterials to Structural Transitions. *Applied Mechanics Reviews* 69, 050801.
- Mina Konaković, Keenan Crane, Bailin Deng, Sofien Bouaziz, Daniel Piker, and Mark Pauly. 2016. Beyond Developable: Computational Design and Fabrication with Auxetic Materials. *ACM Trans. Graph.* 35, 4.
- Yijing Li and Jernej Barbič. 2015. Stable Anisotropic Materials. *IEEE Trans. on Visualization and Computer Graphics* 21, 10, 1129–1137.
- Jianxing Liu and Yihui Zhang. 2018. Soft network materials with isotropic negative Poisson's ratios over large strains. *Soft Matter* 14, 693–703. Issue 5.
- Qiang Lu and Rui Huang. 2009. Nonlinear mechanics of single-atomic-layer graphene sheets. *International Journal of Applied Mechanics* 1, 3, 443–467.
- Jonàs Martínez, Jérémié Dumas, and Sylvain Lefebvre. 2016. Procedural Voronoi Foams for Additive Manufacturing. *ACM Trans. Graph.* 35, 4.
- Jonàs Martínez, Jérémié Dumas, Sylvain Lefebvre, and Li-Yi Wei. 2015. Structure and Appearance Optimization for Controllable Shape Design. *Proc. of ACM SIGGRAPH Asia* 34, 6.
- Jonàs Martínez, Haichuan Song, Jérémié Dumas, and Sylvain Lefebvre. 2017. Orthotropic K-nearest Foams for Additive Manufacturing. *ACM Trans. Graph.* 36, 4.
- Vittorio Megaro, Jonas Zehnder, Moritz Bächer, Stelian Coros, Markus Gross, and Bernhard Thomaszewski. 2017. A Computational Design Tool for Compliant Mechanisms. *ACM Trans. Graph.* 36, 4.
- Eder Miguel, Derek Bradley, Bernhard Thomaszewski, Bernd Bickel, Wojciech Matusik, Miguel A. Otaduy, and Steve Marschner. 2012. Data-Driven Estimation of Cloth Simulation Models. *Comput. Graph. Forum* 31, 2, 519–528.
- Eder Miguel, Rasmus Tamstorf, Derek Bradley, Sara C. Schwartzman, Bernhard Thomaszewski, Bernd Bickel, Wojciech Matusik, Steve Marschner, and Miguel A. Otaduy. 2013. Modeling and Estimation of Internal Friction in Cloth. *ACM Trans. Graph.* 32, 6.
- Matthieu Nesme, Paul G. Kry, Lenka Jeřábková, and François Faure. 2009. Preserving Topology and Elasticity for Embedded Deformable Models. *ACM Trans. Graph.* 28, 3.
- William J. O'Donnell and Bernard F. Langer. 1962. Design of Perforated Plates. *ASME Journal of Engineering for Industry* 84, 3, 307–319.
- Victor Ostromoukhov. 2007. Sampling with Polyominoes. *ACM Trans. Graph.* 26, 3.
- Simon Pabst, Sybille Krzywinski, Andrea Schenk, and Bernhard Thomaszewski. 2008. Seams and Bending in Cloth Simulation. In *Workshop in Virtual Reality Interactions and Physical Simulation "VRIPHYS" (2008)*.
- Julian Panetta, Abtin Rahimian, and Denis Zorin. 2017. Worst-case Stress Relief for Microstructures. *ACM Trans. Graph.* 36, 4.
- Julian Panetta, Qingnan Zhou, Luigi Malomo, Nico Pietroni, Paolo Cignoni, and Denis Zorin. 2015. Elastic Textures for Additive Fabrication. *ACM Trans. Graph.* 34, 4.
- Jesús Pérez, Miguel A. Otaduy, and Bernhard Thomaszewski. 2017. Computational Design and Automated Fabrication of Kirchhoff-plateau Surfaces. *ACM Trans. Graph.* 36, 4.
- Jesús Pérez, Bernhard Thomaszewski, Stelian Coros, Bernd Bickel, José A. Canabal, Robert Sumner, and Miguel A. Otaduy. 2015. Design and Fabrication of Flexible Rod Meshes. *ACM Trans. Graph.* 34, 4.
- Catalin R. Picu. 2011. Mechanics of random fiber networks—a review. *Soft Matter* 7, 6768–6785. Issue 15.
- Hang Jerry Qi and Mary C. Boyce. 2005. Stress-strain behavior of thermoplastic polyurethanes. *Mechanics of Materials* 37, 8, 817–839.
- Ahmad Rafsanjani and Damiano Pasini. 2016. Bistable auxetic mechanical metamaterials inspired by ancient geometric motifs. *Extreme Mechanics Letters* 9, 291–296.
- Christian Schumacher, Bernd Bickel, Jan Rys, Steve Marschner, Chiara Daraio, and Markus Gross. 2015. Microstructures to Control Elasticity in 3D Printing. *ACM Trans. Graph.* 34, 4.
- Christian Schumacher, Bernhard Thomaszewski, and Markus Gross. 2016. Stenciling: Designing Structurally-Sound Surfaces with Decorative Patterns. *Comput. Graphics Forum* 35, 5, 101–110.
- Chengcheng Tang, Xiang Sun, Alexandra Gomes, Johannes Wallner, and Helmut Pottmann. 2014. Form-finding with Polyhedral Meshes Made Simple. *ACM Trans. Graph.* 33, 4.
- Huamin Wang, James F. O'Brien, and Ravi Ramamoorthi. 2011. Data-driven Elastic Models for Cloth: Modeling and Measurement. *ACM Trans. Graph.* 30, 4.
- Jan Wilhelm and Erwin Frey. 2003. Elasticity of Stiff Polymer Networks. *Phys. Rev. Lett.* 91, 108103. Issue 10.
- Hongyi Xu, Funshing Sin, Yufeng Zhu, and Jernej Barbič. 2015. Nonlinear Material Design Using Principal Stretches. *ACM Trans. Graph.* 34, 4.
- Lizhi Xu, Terry C. Shyu, and Nicholas A. Kotov. 2017. Origami and Kirigami Nanocomposites. *ACS Nano* 11, 8, 7587–7599.
- Jonas Zehnder, Stelian Coros, and Bernhard Thomaszewski. 2016. Designing Structurally-sound Ornamental Curve Networks. *ACM Trans. Graph.* 35, 4.
- Jonas Zehnder, Espen Knoop, Moritz Bächer, and Bernhard Thomaszewski. 2017. Metasilicone: Design and Fabrication of Composite Silicone with Desired Mechanical Properties. *ACM Trans. Graph.* 36, 6.
- Kun Zhou, Xin Huang, Xi Wang, Yiyong Tong, Mathieu Desbrun, Baining Guo, and Heung-Yeung Shum. 2006. Mesh Quilting for Geometric Texture Synthesis. *ACM Trans. Graph.* 25, 3, 690–697.

A PERIODIC BOUNDARY CONDITIONS

We incorporate the tileability of a structure patch by defining a set of *periodic boundary conditions* that impose constraints on vertices on opposite boundaries. These boundary conditions guarantee that the patch behaves as if it were surrounded by identical copies of itself, without having to fix the position of vertices, which would artificially stiffen the structure. In the following, we will look at the two cases of planar and curved deformations.

Planar deformation. For planar deformations, the relation of a patch to its virtual neighbors is given by a simple translation, even though locally, there might be out-of-plane deformations of the rods. Since patches are connected at the boundary, we can ensure tileability by guaranteeing that opposite boundaries have the same shape, without restricting the actual shape of the boundary. This requirement can be formulated as a constraint on the difference between corresponding pairs of vertices on opposite boundaries. For any pair of vertices $(\mathbf{x}_i, \mathbf{x}_j)$ on opposite boundaries and a translation \mathbf{d}_{ij} , we can express one of the vertices through the other as

$$\mathbf{x}_j = \mathbf{x}_i + \mathbf{d}_{ij}. \quad (10)$$

The translation \mathbf{d}_{ij} describes the tileability of the patch, and is identical for every pair of vertices on the same pair of boundaries (see Figure 15). We keep this translation as a degree of freedom by choosing a *reference vertex pair* \mathbf{x}_α and \mathbf{x}_β on each boundary pair, and leave their positions unconstrained. We then express the translation as $\mathbf{d}_{ij} = \mathbf{x}_\beta - \mathbf{x}_\alpha$, which ensures that while the distance between two opposite boundaries is free, it is the same for all boundary vertex pairs on corresponding boundaries.

We can then use the vertices \mathbf{x}_α and \mathbf{x}_β , and their counterpart on the other pair of boundaries, to apply macroscopic strains to the structure. Specifically, if we fix the displacement between \mathbf{x}_α and \mathbf{x}_β along a single direction, we impose a *uniaxial strain*.

Curved deformation. We introduce an additional rotation \mathbf{R}_{ij} in the case of curved deformations, and describe the relationship for any vertex pair $(\mathbf{x}_i, \mathbf{x}_j)$ on opposite boundaries as

$$\mathbf{x}_j = \mathbf{R}_{ij}\mathbf{x}_i + \mathbf{d}_{ij}. \quad (11)$$

The rotation \mathbf{R}_{ij} has to be chosen such that the macroscopic curvature of the patch matches the target curvature. For cylindrical curvature configurations with cylinder direction \mathbf{v} and curvature κ_C , we use the difference in rest state positions, $\Delta\mathbf{X}_{ij} = \mathbf{X}_j - \mathbf{X}_i$,

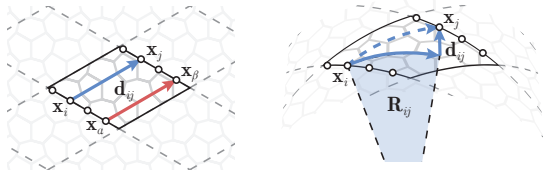


Fig. 15. Planar periodic boundary conditions link all pairs of vertices on opposite boundaries by a translation \mathbf{d}_{ij} (left). For curved configurations, this relation is split into a translation \mathbf{d}_{ij} and rotation \mathbf{R}_{ij} (right).

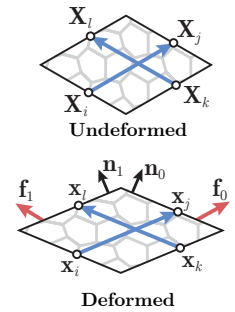
to determine the rotational and translational component: \mathbf{R}_{ij} is a rotation of $\kappa_C \|\Delta\mathbf{X}_{ij} - \mathbf{v}\mathbf{v}^T \Delta\mathbf{X}_{ij}\|$ around \mathbf{v} , and $\mathbf{d}_{ij} = \mathbf{v}\mathbf{v}^T \Delta\mathbf{X}_{ij}$.

In the case of the spherical curvature κ_S , we only use rotations to define the relationship between the vertices, and set $\mathbf{d}_{ij} = \mathbf{0}$. The rotation \mathbf{R}_{ij} is then defined as the rotation of $\kappa_S \|\Delta\mathbf{X}_{ij}\|$ around the rotation axis aligned with $(\mathbf{X}_i + (0, 0, 1/\kappa_S)^T) \times \Delta\mathbf{X}_{ij}$, which puts the macroscopic deformation onto a sphere with the desired curvature, but violates the strict tileability of the structure.

B COMPUTING THE MACROSCOPIC IN-PLANE STRAIN AND STRESS

The macroscopic strain and stress of a simulation with periodic boundary conditions can conveniently be extracted from the deformations and forces at the boundaries.

In particular, we can consider two pairs of vertices $(\mathbf{x}_i, \mathbf{x}_j)$ and $(\mathbf{x}_k, \mathbf{x}_l)$ on different opposing boundaries (see inset). The deformations of these vertices relative to each other directly describe the deformation of the boundary, and with that the macroscopic deformation. In terms of the macroscopic deformation gradient, this relationship is given by $\mathbf{x}_i - \mathbf{x}_j = \mathbf{F}_{macro}(\mathbf{X}_i - \mathbf{X}_j)$, where \mathbf{X}_i is the undeformed position of \mathbf{x}_i . By using the two pairs of vertices, we can set up a system of equations whose solution is the macroscopic deformation gradient:



$$\mathbf{F}_{macro} = [\mathbf{x}_i - \mathbf{x}_j \quad \mathbf{x}_k - \mathbf{x}_l] [\mathbf{X}_i - \mathbf{X}_j \quad \mathbf{X}_k - \mathbf{X}_l]^{-1} \quad (12)$$

From this expression, we then compute the macroscopic Cauchy strain tensor as $\epsilon_{macro} = \frac{1}{2}(\mathbf{F}_{macro} + \mathbf{F}_{macro}^T) - \mathbf{I}$.

Similarly, we can compute the macroscopic stress by looking at the forces at the boundary of the simulation domain. For two non-opposing boundaries, we compute the forces per unit length \mathbf{f}_0 and \mathbf{f}_1 . Then, using the boundary normals \mathbf{n}_0 and \mathbf{n}_1 , which are perpendicular to $\mathbf{x}_j - \mathbf{x}_k$ and $\mathbf{x}_l - \mathbf{x}_i$, respectively, we derive a system of equations based on the stress equation $\mathbf{f} = \boldsymbol{\sigma}_{macro}\mathbf{n}$, and obtain

$$\boldsymbol{\sigma}_{macro} = [\mathbf{f}_0 \quad \mathbf{f}_1] [\mathbf{n}_0 \quad \mathbf{n}_1]^{-1}. \quad (13)$$